

HiSST: 4th International Conference on High-Speed Vehicle Science Technology

22-26 September 2025, Tours, France



Resolvent and sensitivity analysis for investigating and delaying linear instabilities in quiet hypersonic wind tunnel nozzles

H. Lemarquand ¹, M. Lugrin ¹, C. Content ², C. Caillaud ³, S. Esquieu ³, D. Sipp ⁴

Abstract

Base-flow computations, resolvent, and sensitivity analyses are performed for a hypersonic wind tunnel nozzle at Mach 6. This research precisely identifies, through resolvent analysis, the locations and mechanisms governing the development of the Görtler instability, as well as the first and second Mack modes, within a hypersonic wind tunnel nozzle. Additionally, sensitivity analysis of the resolvent optimal gain provides a pathway to mitigate instability growth, and consequently delay the transition, through wall temperature variation. This methodology can be extended to other forms of control, such as nozzle wall displacement and other key control parameters. Using the sensitivity results, an optimal profile is also designed to simultaneously control several unstable modes. These findings contribute to the advancement of quiet wind tunnels and ground testing facilities for hypersonic flows.

Keywords: Hypersonic flow, Transition, Boundary layer stability, Resolvent, Sensitivity, Wind-Tunnel, Nozzle, Optimisation

1. Introduction

During the design phase of hypersonic vehicles, wind-tunnel testing plays a critical role in validating and studying key factors such as aerodynamic performance, laminar-to-turbulent transition of the boundary layer on the test model, etc. Accurate prediction of this transition is crucial as the turbulent boundary layer leads to a significant increase in wall heat flux. However, the vast majority of current hypersonic wind tunnels are not sufficiently representative of atmospheric flight conditions, particularly in terms of enthalpy and freestream noise levels [1]. This study specifically focusses on reducing fluctuation in the test section (="noise level") of these facilities to support the development of quiet hypersonic wind tunnels. Such fluctuations are important to study because they drastically alter the laminar-to-turbulent transition of the boundary layer on the test model due to the receptivity process [2]. There can be various sources of these disturbances in wind tunnels [1], but above Mach 2.5 the primary source of noise is the eddy-Mach-wave radiation from the turbulent boundary layer that develops on the nozzle wall [3]. This noise is around 1 to 2 orders of magnitude above flight levels [1, 4]. Therefore, one of the main issues in quiet hypersonic wind tunnels is to control the laminar-to-turbulent transition of the boundary layer on the nozzle wall. Such quiet wind tunnels, in which the laminarity of the boundary layers along the wall is maintained to significantly reduce the noise levels, do exist for Reynolds numbers up to $20 \times 10^6 \, \text{m}^{-1}$ at Mach 6 (e.g. BAM6QT at Purdue) [1]. However, such facilities are rare, non-existent in Europe [4], and remain limited in both Mach and Reynolds numbers [1, 5].

This research does not aim to investigate the nonlinear interactions that lead to transition, but rather to identify the linear instabilities present in the boundary layer and explore ways to reduce their growth in order to delay the transition along the nozzle wall. A sketch of all potential instabilities in hypersonic nozzle flows is provided in Fig. 1. First, Görtler instability can arise over the concave walls of the nozzle [6]. This instability occurs across all Mach numbers, from incompressible to hypersonic flow conditions, and results from a centrifugal instability mechanism related to the concave curvature of the streamlines [7]. Görtler instability is known to be significant and is considered in wind tunnel nozzle design [1, 8, 9]. A second class of instabilities is composed of the first and second Mack modes. Stability analysis has

¹DAAA ONERA, Institut Polytechnique de Paris, 92190, Meudon, France

² DAAA ONERA, Institut Polytechnique de Paris, 92320, Châtillon, France

³CEA-CESTA, 15 Avenue des Sablières, 33114, Le Barp, France

⁴ONERA, Institut Polytechnique de Paris, 91120, Palaiseau, France

Fig 1. Schematic of all instabilities within a hypersonic nozzle.

shown that such instabilities can grow within hypersonic wind tunnel nozzles [8, 10]. The oblique first Mack mode corresponds to a viscous inflectional mode, in which fluctuations are localised around the generalised inflection point (GIP). In addition to this viscous first mode, Mack [11] found that multiple inviscid instability modes can exist in the supersonic boundary layer, referred to as the second Mack mode and higher-order modes. The second Mack mode corresponds to a 2D trapped acoustic wave close to the wall and becomes unstable above $M \approx 4$ [11]. Lastly, recirculation bubbles can form at the convergent inlet [12] or at the suction lip upstream of the nozzle throat [13]. These bubbles can lead to new instabilities including exponential instability (global modes) [14] and non-normal input-output amplification (resolvent mode) such as the Kelvin-Helmholtz (KH) instability that arises from the separated shear layer [15].

In this study, the global linear stability tool [16, 17] is chosen to provide valuable insights on the development of instabilities and to support nozzle optimisation. There are four main reasons why global stability analysis is chosen over local stability methods (which are currently used in the design of quiet hypersonic wind tunnels [8, 18]) in this study. First, local stability analyses are difficult to apply in complex configuration, such as when the nozzle includes a suction lip upstream of the throat. Second, local approaches rely on the assumption that the flow is quasi-parallel, an assumption that may fail in regions with strong pressure gradients, flow separation, or high wall curvature, conditions commonly encountered in nozzle flows. Third, local methods completely fail to capture global modes in the flow. As a result, relying solely on local stability methods to optimise quiet wind tunnel nozzles can lead to suboptimal designs due to an incomplete physical representation of the instability mechanisms. So, to address more general configuration and have more information on the various instabilities, we have chosen to use global stability analysis. This framework relies solely on the assumption of linearity, thus the non-parallel effects are fully accounted for. Additionally, this method also takes into account the non-modal phenomena arising from the non-normality of the Navier-Stokes operator [19]. Moreover, these methods provide direct access to the gradients of various flow quantities, such as the sensitivity of the resolvent optimal gain. This enables the identification of regions where small modifications to the base-flow have the most significant impact on flow stability [20, 21, 22].

The global linear stability analysis of the hypersonic nozzle flow was already performed in one of our previous studies [23], allowing detailed identification and characterisation of all the instability mechanisms shown in Fig. 1 and discussed above (including both global and resolvent modes). Therefore, in the present study, we will only briefly revisit the analysis of these modes and instead focus on the sensitivity results of the resolvent mode. The objective of this study is to compute and validate the sensitivity of the resolvent optimal gain, in order to identify pathways for mitigating instability growth, and consequently delaying the transition, through control method: variations in wall temperature, nozzle wall displacement, and other key parameters. These sensitivity results will serve, in future work, as optimal gradients to inform gradient-based optimisation strategies. Thereby supporting the development of next-generation quiet wind tunnels and advanced ground testing facilities for hypersonic flows.

2. Methods

2.1. Governing equations

The objective of this section is to introduce the wall control parameter methods (such as wall temperature variation, suction/blowing, etc.) applied to a small 3D perturbations (called resolvent modes) that

develop around a 2D base-flow due to the presence of a forcing term in the flow domain ($f_r \neq 0$). The amplification of these resolvent modes at specific frequencies arises from the non-normality of the Jacobian operator \mathcal{J} [16], and can occur even if the flow is globally stable. These instabilities depend on receptivity mechanisms and thus require external forcing ($f_r \neq 0$) to be amplified. The flow is governed by the compressible Navier-Stokes equations written in conservative form, in the cylindrical coordinate system (x, r, θ) (axisymmetric nozzle):

$$\begin{cases} \partial_t q_t = R(q_t) + Pf_t, \\ B(q_t, p_c)(x) = 0. \end{cases}$$
 (1)

with q_t the state vector of conservative variables, R(q) the discrete residual, f_t a small amplitude harmonic forcing term (P is a prolongation matrix used to restrict the domain or components of the forcing field) and B the boundary condition (for example, the isothermal wall). The wall control parameter $p_C = p_0 + \epsilon Cp$ is invariant in time and in θ -direction as the base-flow is assumed to remain steady and 2D [21]. Here, $p_0 = 0$ as the control is not at the same order than the base-flow, and C is a vector used to select the control component, so the following section can be applied either to temperature control or wall suction/blowing control or other wall control parameters. In this study, we will use the "weakly nonlinear formalism" approach introduced by Kitzinger [24] to derive the sensitivity of the solution, rather than using the traditional adjoint or Lagrangian-based methods. This choice facilitates the mathematical treatment of wall deformation, which will be addressed in subsequent work. It is important to note that "weakly nonlinear" here refers to interactions at infinitesimal orders of magnitude and does not imply magnitudes large enough to cause nonlinear effects that would prevent the use of linear theory. The first objective is to recover the sensitivity results previously obtained via the Lagrangian approach by Poulain et al. [21], but now using this alternative formalism. In this context, the total solution and volume forcing are expanded as follows:

$$q_{t}(\vec{x},t) = \overline{q}(x,y) + \epsilon \left(\check{q}_{r}(x,y) e^{i(m\theta + \omega t)} + c.c. + \check{q}_{c} \right) + \epsilon^{2} \left(\check{q}_{i}(x,y) e^{i(m\theta + \omega t)} + c.c. + ... \right) + o(\epsilon^{2}),$$

$$(2)$$

$$f_{t}(x,y,z,t) = \epsilon \left(\check{f}_{r} e^{i(m\theta + \omega t)} + c.c. \right) + \epsilon^{2} \left(\check{f}_{i} e^{i(m\theta + \omega t)} + c.c. \right),$$

$$(3)$$

where, \overline{q} is the 2D base-flow, define as $R_T(\overline{q}) = 0$ (see § 2.2.1.). $\check{q}_r(x,y) e^{i(m\theta+\omega t)}$ is the response to volume forcing $\check{f}_r e^{i(m\theta+\omega t)}$ (classic resolvent, see § 2.2.2.). \check{q}_c is the response to the wall control parameter p_c . $\check{q}_i(x,y) e^{i(m\theta+\omega t)}$ is the perturbation due to the nonlinear interaction of (q_r,q_c) , and $\check{f}_i e^{i(m\theta+\omega t)}$ is the associated forcing. And, "..." gathers all the interaction terms that are not proportional to $e^{i(m\theta+\omega t)}$ (higher-order harmonic). The objective now is to derive the equations governing the linear dynamics of the system in response to the forcing and its associated flow response. To achieve this, we linearise Eq. (1) around the base-flow, as perturbations are assumed to be small, i.e., $\|\epsilon q'\| \ll \|\overline{q}\|$.

2.1.1. Development of the residual equation

We perform a Taylor expansion of R around the base-flow \overline{q} . Expanding to order $\varepsilon = o(\varepsilon^2, e^{i(m\theta + \omega t)})$ yields:

$$\partial_t q_t = R(\overline{q}) + (\nabla_q R|_{\overline{q}})(q_t - \overline{q}) + \frac{1}{2}(\nabla_{q,q} R|_{\overline{q}})(q_t - \overline{q}, q_t - \overline{q}) + Pf_t$$

$$\Leftrightarrow \epsilon i\omega \check{q}_r e^{i(m\theta + \omega t)} + \epsilon^2 i\omega \check{q}_i e^{i(m\theta + \omega t)} + c.c = R(\overline{q})$$
(4)

$$+\epsilon \left[(\nabla_{q}R|_{\overline{q}})_{m}\check{q}_{r} e^{i(m\theta+\omega t)} + (\nabla_{q}R|_{\overline{q}})_{0}\check{q}_{c} \right] + \epsilon^{2} (\nabla_{q}R|_{\overline{q}})_{m}\check{q}_{i} e^{i(m\theta+\omega t)}$$

$$+\epsilon^{2} e^{i(m\theta+\omega t)} (\nabla_{q,q}R|_{\overline{q}})_{m}^{0} (\check{q}_{r}, \check{q}_{c}) + \epsilon P \check{f}_{r} e^{i(m\theta+\omega t)} + \epsilon^{2} P \check{f}_{i} e^{i(m\theta+\omega t)} + c.c. + ... + o(\epsilon^{2})$$
 (5)

where, $(\nabla_q R|_{\overline{q}})_0$ is the Jacobian written with $\partial_z = 0$ (i.e. 2D Jacobian), $(\nabla_q R|_{\overline{q}})_m$ is the Jacobian written with $\partial_z \to im$ (i.e. 3D Jacobian), $(\nabla_{q,q} R|_{\overline{q}})_m^0$ is the Hessian but with $\partial_z \to im$ in the first term and $\partial_z = 0$ for the second term. By identification in the two developments, i.e. by identification in the Taylor development (ϵ by ϵ) and the Fourier development (harmonic by harmonic):

$$\begin{cases} \varepsilon = o(0,0) : R(\overline{q}) = 0, \\ \varepsilon = o(1,0) : (\nabla_{q}R|_{\overline{q}})_{0}\check{q}_{c} = 0, \\ \varepsilon = o(1,e^{i(m\theta+\omega t)}) : i\omega\check{q}_{r} = (\nabla_{q}R|_{\overline{q}})_{m}\check{q}_{r} + P\check{f}_{r}, \\ \varepsilon = o(2,e^{i(m\theta+\omega t)}) : i\omega\check{q}_{i} = (\nabla_{q}R|_{\overline{q}})_{m}\check{q}_{i} + (\nabla_{q,q}R|_{\overline{q}})_{m}^{0}(\check{q}_{r},\check{q}_{c}) + P\check{f}_{i}, \end{cases}$$

$$(6)$$

2.1.2. Development of the boundary condition

We perform also a Taylor expansion of B around the base-flow (\overline{q}, p_0) . By developing with $\varepsilon = o(\varepsilon^2, e^{i(m\theta + \omega t)})$:

$$\left[B(\overline{q}) + \epsilon \left((\nabla_{q}B|_{\overline{q}})\check{q}_{r} e^{i(m\theta + \omega t)} + c.c. + (\nabla_{q}B|_{\overline{q}})\check{q}_{c} + (\nabla_{p}B|_{\overline{q}})Cp \right) + \epsilon^{2} \left((\nabla_{q}B|_{\overline{q}})\check{q}_{i} e^{i(m\theta + \omega t)} + (\nabla_{q,p}B|_{\overline{q}})(\check{q}_{r}, Cp) e^{i(m\theta + \omega t)} + c.c. \right) + \dots \right] (x) = 0$$
(7)

By identification in the two developments, i.e. by identification in the Taylor development (ϵ by ϵ) and the Fourier development (harmonic by harmonic):

$$\begin{cases}
\varepsilon = o(0,0) : B(\overline{q}) = 0 \\
\varepsilon = o(1,0) : (\nabla_{q}B|_{\overline{q}})\check{q}_{c} + (\nabla_{p}B|_{\overline{q}})Cp = 0 \\
\varepsilon = o(1,e^{i(m\theta+\omega t)}) : (\nabla_{q}B|_{\overline{q}})\check{q}_{r} = 0 \\
\varepsilon = o(2,e^{i(m\theta+\omega t)}) : (\nabla_{q}B|_{\overline{q}})\check{q}_{i} + (\nabla_{q,q}B|_{\overline{q}})(\check{q}_{r},\check{q}_{c}) + (\nabla_{q,p}B|_{\overline{q}})(\check{q}_{r},p) = 0
\end{cases}$$
(8)

2.2. Base-flow, Resolvent analysis and Sensitivity analysis

2.2.1. Base-flow equation

The equation at $\varepsilon = (0, 0)$ in (6) & (8) corresponds to the base-flow \overline{q} , which is a steady solution of the governing equation satisfying $R_T(\overline{q}) = 0$. Hereafter, the notation $(\cdot)_T$ will be used to denote the total residual, including both the residual R and the application of boundary conditions B.

2.2.2. Resolvent analysis - Forcing/Response equation

The equation at $\varepsilon=(1,e^{i(m\theta+\omega t)})$ in (6) & (8) corresponds to the input/output problem: $\check{q}_r=\mathcal{R}_{\omega,m}P\check{f}_r$, where, $\mathcal{R}_{\omega,m}=(i\omega I-\mathcal{J}_m)^{-1}$ is the input volume force Resolvent, and $\mathcal{J}_m=(\nabla_q R_T|_{\overline{q}})$ is the 3D Jacobian of the total residual. This resolvent operator represents a linear transfer function between the incoming forcing \check{f}_r (input) and the flow response \check{q}_r (output). Note that the Jacobian operator $\mathcal{J}(m)$ depends on the azimuthal number m to analytically account for the θ -direction, thereby extending the flow stability analysis to 3D, for more details refer to [25, 23]. Then, for a given (ω,m) , the most amplified resolvent modes is found by solving an optimisation problem defined as a ratio between two energy: $\mu^2=\sup_{\check{f}}\left(\|\check{q}_r\|_E^2/\|\check{f}_r\|_F^2\right)$, where μ^2 is the gain, $\|\cdot\|_E$ and $\|\cdot\|_F$ are the norms used to evaluate the energy amplitude of \check{q}_r and \check{f}_r . Using a discrete scalar product norm, these norms can be expressed with their Hermitian matrix Q_E and Q_F such as $\|\check{q}\|_E^2=\check{q}^*Q_E\check{q}$ and $\|\check{f}\|_F^2=\check{f}^*Q_F\check{f}$, where \check{q}^* is the conjugate transpose of \check{q} . The Chu energy norm is used to account for the compressibility effects in the energy measure [26]. The resulting optimisation problem can be viewed as a Rayleigh quotient and can be recast as a generalised Hermitian eigenvalue problem:

$$P^* \mathcal{R}_{\omega,m}^* Q_E \mathcal{R}_{\omega,m} P \check{f}_{r,i}^{opt} = \mu_i^2 Q_F \check{f}_{r,i}^{opt}, \tag{9}$$

where μ_i^2 , $i \in [[0, \dots]]$, are the eigenvalues sorted by energy such that $\mu_i^2 \ge \mu_{i+1}^2$. The $\check{f}_{r,i}^{opt}$ are the optimal forcing, while $\check{q}_{r,i}^{opt} = \mathcal{R}P\check{f}_{r,i}^{opt}$ are the optimal responses. This eigenvalue problem (9) allows to map the linear system amplification of the base-flow by solving it for a range of (ω, m) .

2.2.3. Control equation

The equation at $\varepsilon = (0, e^{i(m\theta + \omega t)})$ in (6) & (8) corresponds to the control/response problem: $\check{q}_c = \mathcal{R}_{0,0}\mathcal{P}_{\mathcal{W}\overline{q}}Cp$, where, $\mathcal{R}_{0,0}$ is the Resolvent at 0 frequency and 0 azimuthal wavenumber. $\mathcal{P}_{\mathcal{W}\overline{q}} = (\nabla_p R_T|_{\overline{q}})_0$ goes form wall quantities to q in the volume.

2.2.4. Non-linear interaction equation

The equation at $\varepsilon = (2, e^{i(m\theta+\omega t)})$ in (6) & (8) corresponds to the response equation due to the non-linear interaction of (q_r, q_c) : $\check{q}_i = \mathcal{R}_{\omega,m}\mathcal{H}^0_{m,\check{q}_r}\check{q}_c + \mathcal{R}_{\omega,m}P\check{f}_i + \mathcal{R}_{\omega,m}\mathcal{P}_{\mathcal{W}\overline{q},\check{q}_r}\mathcal{C}p$. where, $\mathcal{H}^0_m(\check{q}_r, \check{q}_c) = (\nabla_{q,q}R_T|_{\overline{q}})(\check{q}_r, \check{q}_c)$ is the Hessian of the total residual, such as $\mathcal{H}^0_m(\check{q}_r, q) = \mathcal{H}^0_{m,\check{q}_r}q$, $\forall q$. And, $\mathcal{P}_{\mathcal{W}\overline{q},\check{q}_r} = (\nabla_{q,p}R_T|_{\overline{q}})^0_{m,\check{q}_r}$ is the Hessian that goes from wall quantities to q in the volume, such as $(\nabla_{q,p}B|_{\overline{q}})(\check{q}_r, p) = (\nabla_{q,p}B|_{\overline{q}})_{,\check{q}_r}p$, $\forall p$. Note that the Hessian operator depends on the azimuthal wavenumber m to analytically account for the θ -direction [25, 23].

2.2.5. Sensitivity analysis - Full gain expansion

To derive the sensitivity expression of the optimal resolvent gain, we define a new gain G (as introduced in § 2.2.2.) based on the harmonic $e^{i(m\theta+\omega t)}$. It is important to note that variations of the metric Q are also accounted for, since Q is defined with respect to the total solution q_t . Therefore: $Q(q_t) = Q(\overline{q}) + \epsilon \delta Q + o(\epsilon, e^{i0\times (m\theta+\omega t)})$ with $\delta Q = \partial_q (Q\check{q}_c)|_{\overline{q}}$. The expansion is truncated at this order so that G includes only harmonics of the same order (higher order harmonics are neglected in the expansion). Consequently, the full gain expansion for the harmonic $e^{i(m\theta+\omega t)}$ is:

$$G^{2} = \frac{(\check{q}_{r} + \epsilon \check{q}_{i})^{*} (Q_{E} + \epsilon \delta Q_{E})(\check{q}_{r} + \epsilon \check{q}_{i})}{(\check{f}_{r} + \epsilon \check{f}_{i})^{*} (Q_{F} + \epsilon \delta Q_{F})(\check{f}_{r} + \epsilon \check{f}_{i})}$$
(10)

After a mathematical development using a Taylor expansion of 1/(1+x), as well as the normalisation condition $\check{f}_r^*Q_F\check{f}_r=1$, we obtain the following expression:

$$G^{2} = \mu^{2} + \epsilon \left[2 \operatorname{Re} \left(\check{q}_{r}^{*} Q_{E} \check{q}_{i} - \mu^{2} \check{f}_{r}^{*} Q_{F} \check{f}_{i} \right) + \check{q}_{r}^{*} \delta Q_{E} \check{q}_{r} - \mu^{2} \check{f}_{r}^{*} \delta Q_{F} \check{f}_{r} \right]$$

$$(11)$$

We finally obtain an expression of the following form:

$$G^{2}(p) = G^{2}(0) + (\nabla_{p}G^{2})^{*}Q_{p}p, \tag{12}$$

with $G^2(0)=\mu^2$, i.e. an expression that gives the new optimal resolvent gain G^2 (after control) as a function of the previous gain μ^2 (without control p=0) and the gain gradient (which corresponds to the sensitivity of the solution). In the above expression, Q_p denotes the scalar product associated with wall-parameter control variations p, defined as: $\langle p_a, p_b \rangle_{Q_p} = p_a^* Q_p p_b = \int_{\Gamma_{\mathcal{W}}} \overline{p_a}(s) p_b(s) \, ds$. Using the results from § 2.2.2., 2.2.3. and 2.2.4., it is then possible to show that Eq. (11) leads to:

$$\frac{\nabla_p G^2}{\mu^2} = Q_p^{-1} \left[\mathcal{P}_{\mathcal{W}} \frac{*}{q} Q_{f_c} \frac{\nabla_{f_c} G^2}{\mu^2} + \frac{2}{\mu^2} \operatorname{Re} \left(\mathcal{P}_{\mathcal{W}} \frac{*}{q, \check{q}_r} \mathcal{R}_{\omega, m}^* Q_E \check{q}_r \right) \right], \text{ with,}$$
 (13)

$$\frac{\nabla_{f_c}G^2}{\mu^2} = -Q_{f_c}^{-1}P^*\mathcal{J}_0^{-1*} \left[\frac{2}{\mu^2} \operatorname{Re}\left((\mathcal{H}_{m,\check{q}_r}^0)^* \mathcal{R}_{\omega,m}^* Q_E \check{q}_r \right) + \frac{1}{\mu^2} \left(\frac{\partial (Q_E \check{q}_r)}{\partial q} \right)^* \check{q}_r - \left(\frac{\partial (Q_F \check{f}_r)}{\partial q} \right)^* \check{f}_r \right]$$
(14)

where, $\nabla_p G^2/\mu^2$ represents the sensitivity of the optimal resolvent gain to a wall control parameter control p, and $\nabla_{f_c} G^2/\mu^2$ corresponds to the sensitivity to a volume forcing. Therefore, we recover exactly the result obtained by Poulain et al. [21], but using a different formalism which will allow us to introduce more easily wall displacement control. Indeed, for wall displacement control, it is sufficient to modify the wall boundary condition in Eq. (1) by applying a perturbation $\epsilon h = \epsilon (h_x, h_r, h_\theta)^T$, which corresponds to a wall deformation that controls the flow. This condition is expressed as: $B(q_t, \vec{x}_0 + \epsilon h) = 0$ where \vec{x}_0 denotes the initial position of the wall (i.e. the base-flow). In analogy to the wall control parameter p_c , we obtain the same total solution and forcing from Eqs. (2) and (3), but this time controlled by a wall displacement of ϵh . By applying the same mathematical reasoning as before, we can derive an expression for the sensitivity of the solution with respect to wall displacement.

2.2.6. Numerical methods

In this study, the open-source CFD code BROADCAST [25] is used. This toolbox provides all the tools and numerical methods needed to compute the base-flow and the discrete operators (using Algorithmic

Fig 2. Base-flow Mach number field. Zoom: recirculation bubble at the convergent inlet.

Differentiation (AD), the AD tool accurately computes the n-order derivatives of the various operators needed in this study), as well as to perform global linear stability analysis of 2D Cartesian or axisymmetric flows. For more information on this code (structured high-order scheme used, AD, methods, etc.) refer to Poulain et al. [25], and for validation of this code see [25, 27, 23].

For the boundary condition: inlet = subsonic stagnation inlet (P_t , T_t), outlet = extrapolate order 0, axis = axisymmetric condition, wall = isothermal wall at T_{wall} . Note that before the isothermal wall a very small zone (1% of the settling chamber length $l_{settling} = 0.2~m$) is added to ensure a smooth variation between the inlet boundary condition T_t and the wall temperature T_{wall} using a tanh function for the wall boundary condition. The base-flow obtained ($N_x \times N_r = 5780 \times 400$) is converged with a decrease close to 12 orders of magnitude of the L^2 norm of the residuals. For further details on the numerical setup (including the mesh, base-flow convergence, and other implementation aspects), the reader is referred to the detailed description provided in our previous study [23].

3. Baseflow computation

The geometry of the hypersonic wind tunnel nozzle used in this study is shown in Fig. 2. It is an axisymmetric nozzle from ONERA at a Mach number of 6. The nozzle consists of three parts: the settling chamber, the convergent, and the divergent. Note that the settling chamber length has been increased to accommodate the inlet boundary condition, the dimensions used in this study are therefore not exactly representative of the real configuration. Nevertheless, this part can be seen as a simplified model of a real settling chamber commonly used in this type of wind tunnel. The value of the boundary condition used is summarised in here : $P_t = 4$ bar, $T_t = 550$ K, $T_{iso} = 300$ K, $M_{\infty} = 6.0$, $Re_{\infty} = 2.8 \cdot 10^6$ m⁻¹.

The evolution of the Mach number of the base-flow is shown in Fig. 2. An boundary layer separation is observed at the convergent inlet. This flow feature is important because recirculation bubbles can trigger global modes and resolvent modes. The presence of this recirculation bubble here is likely because this wind tunnel was designed to operate at higher stagnation pressures than those used in this study.

4. Resolvent analysis

The resolvent analysis of the nozzle flow is conducted to investigate resolvent modes. A detailed study of all resolvent and global modes throughout the nozzle was presented in our previous work [23]. Here, we provide only a brief identification, as the main objective is to focus on the sensitivity analysis and its validation. This previous study showed that the base-flow is globally unstable due to the recirculation bubble at the convergent section inlet. As a result, the resolvent analysis would typically not be valid in such a case, since such analyses are normally performed on a globally stable flow (i.e. the Jacobian does not exhibit unstable eigenvalues) [16]. However, our goal here is not to characterise the exact transition mechanism, but rather to validate sensitivity tools to evaluate the gradient to optimise these nozzles in a complex configuration. Additionally, in our case, we limit our analysis to the divergent section of the nozzle, deliberately avoiding the upstream region. The latter is assumed to be stabilised via an appropriately designed and implemented suction lip. Under this assumption, resolvent analysis is applied to examine how such flow would behave if there were no global unstable mode.

For this resolvent analysis, the restriction matrix P (see Eq. (9)) is used to limit the forcing to the region where $x \ge 0.4$ m, a domain that includes both the throat and the divergent section of the nozzle. This setup reflects a realistic configuration for quiet wind tunnel design, where a suction lip is assumed to stabilise the upstream flow. In such cases, the primary objective is to mitigate instabilities downstream of the suction lip (see Fig. 1). Fig. 3, shows the evolution of the optimal gain $\mu_0^2 = \|\check{q}_{opt,0}\|_E^2 / \|\check{f}_{opt,0}\|_F^2$ as a function of (f,m). Three regions of maximum gain can be observed, indicating four dominant mechanisms: the Görtler instability, the first and second Mack modes.

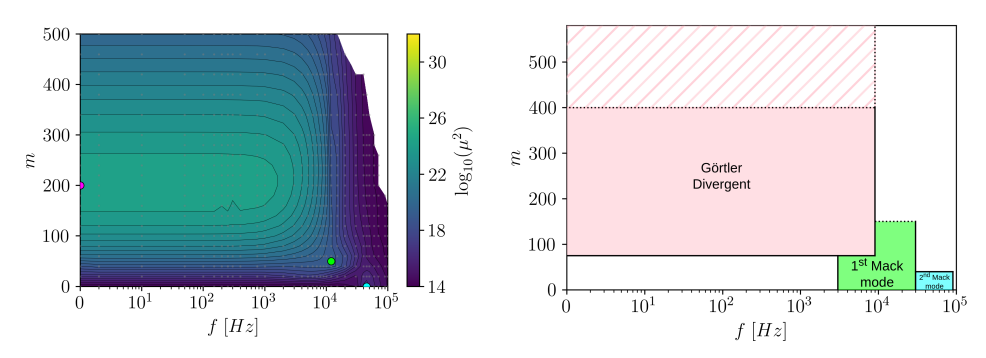


Fig 3. (Left): Optimal gain map μ_0^2 in (f, m) space with the forcing field restricted to $x \ge 0.4 \, m$. (•): Görtler instability peak. (•): first and (•): second Mack mode peak. (Right): Simplified overview.

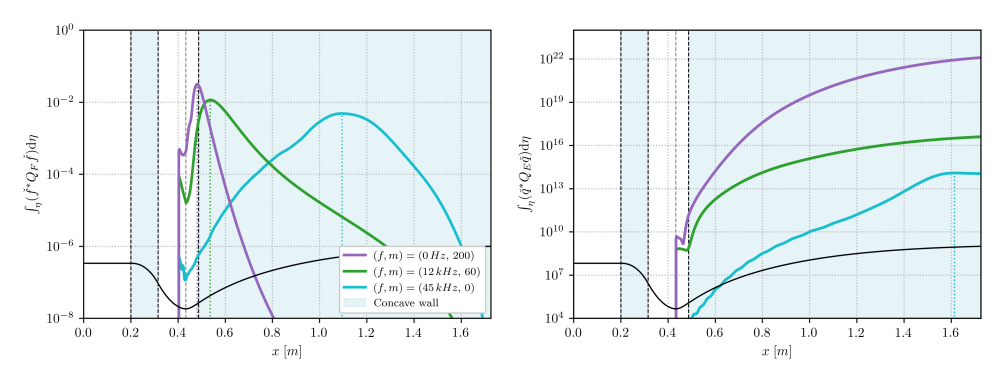


Fig 4. (—) Evolution of the quantity E_{Chu} of the optimal forcing (left) and response (right) computed along the gridlines in the r-direction by integrating the local Chu energy contribution. (f, m) = (0 Hz, 200): Görtler instability. (f, m) = (12 kHz, 60): first Mack mode. (f, m) = (45 kHz, 0): second Mack mode.

Fig. 4 shows the streamwise evolution of E_{Chu} [26], computed along the wall normal direction for the three leading mechanisms. Blue areas indicate where the flow is unstable and can develop centrifugal instabilities since the Rayleigh discriminant $\Delta < 0$ [28], these zones correspond exactly to the regions with concave wall: the first part of the convergent and the second part of the divergent (see Fig. 2). The first region does not affect stability since the analysis is downstream. The first identified mechanism is the stationary Görtler instability, peaking at m = 200, and constitutes the dominant mechanism. The wall curvature due to the relatively short design of the nozzle induces this centrifugal instability. Fig. 4 shows that the forcing peak upstream of the concave part of the divergent section, and the response peak at the divergent exit, with response growth occurring in concave regions ($\Delta < 0$). Unlike Lemarquand et al. [23], the optimal gain map exhibits a single "bump" as the instability develops only in one concave region where $\Delta < 0$. The second mechanism is the second Mack mode, axisymmetric (m = 0) around $f \approx 45$ kHz, consistent with Mack [11] estimation $f = U_e/2\delta$. It is the least amplified instability here, which is consistent with findings from previous Mach 6 wind tunnel investigations [8, 10]. Indeed, this mode is known to develop above $M \approx 4$ [11], a condition reached in a limited portion of the divergent section due to the short length of the studied nozzle. The third identified mechanism is the first Mack mode, which peaks around (f, m) = (12 kHz, 60). As (f, m) are non-zero, this corresponds to an oblique mode. From the resolvent analysis, the N factors of each instability can be computed using the definition provided by [29]. We obtain: $N_{\text{q\"ortler}} = 13.0$, $N_{\text{1st mode}} = 6.37$ and $N_{\text{2nd mode}} = 4.07$.

5. Wall temperature sensitivity analysis

Having identified the dominant resolvent modes, we compute their sensitivity to nozzle wall temperature by solving Eq.(13) with p=T for each leading mode. Since the objective is to reduce their amplification (i.e. to achieve $G^2 < \mu^2$, see Eq. (12)), we examine in Fig. 5 the opposite of the sensitivity of the optimal resolvent gain, defined as $-(\nabla_T G^2/\mu^2)$. A positive value indicates that increasing the wall temperature of the base-flow would help stabilise the mode, whereas a negative value suggests that decreasing the wall temperature would be beneficial. This figure therefore represents the optimal wall temperature gradient required to mitigate the growth of flow instabilities.

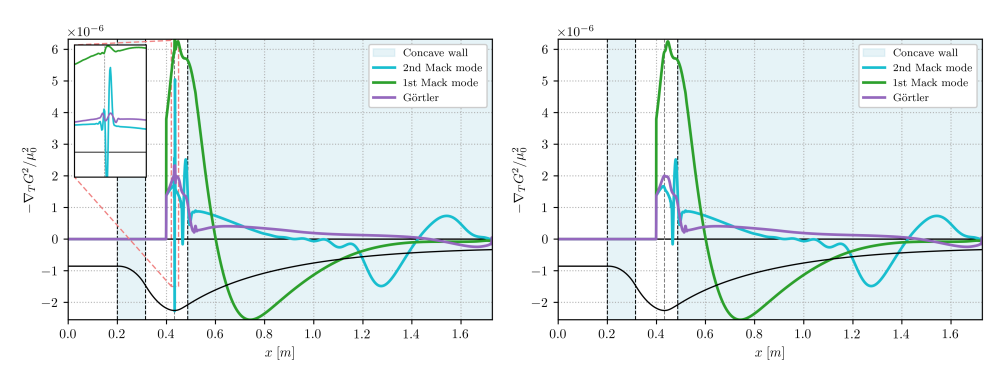


Fig 5. (Left): Optimal wall temperature control profile to damp the three main instabilities, i.e. opposite of the sensitivity of the optimal resolvent gain for the three dominant instabilities: $-(\nabla_T G^2/\mu^2)$, since the objective is to achieve $G^2 < \mu^2$ in Eq. (12). (Right): Smoothed control profile near the throat region. First Mack mode at $(f, m) = (12 \, \text{kHz}, 60)$, second Mack mode at $(f, m) = (45 \, \text{kHz}, 0)$, Görtler instability at $(f, m) = (0 \, \text{Hz}, 200)$.

The strong oscillations observed near the nozzle throat, particularly for the second Mack mode (Fig. 5), are subsequently smoothed in order to derive a more practically feasible temperature control profile from the sensitivity analysis. Indeed, such abrupt temperature variations would be extremely difficult to implement in an experimental setup. During the gradient validation step, we quantify the performance loss associated with this smoothing and demonstrate that it has only a limited impact on the reduction of the resolvent gain. An explanation for the origin of these oscillations is provided in § 7...

We observe that heating the wall near the nozzle throat contributes to the stabilisation of all three dominant resolvent modes. However, further downstream, the different instability mechanisms begin to compete with each other. Among these modes, the first Mack mode is found to be the most sensitive to wall temperature control ($\|\nabla_T G^2\|_{1st \text{ mode}}^2 > \|\nabla_T G^2\|_{2nd \text{ mode}}^2 > \|\nabla_T G^2\|_{G\"ortler}^2$). Whereas, the G\"ortler instability is the least sensitive, consistent with the findings of Schneider [8]. For the first Mack mode, our results align with the behaviour described by Mack [30], who demonstrated that a uniformly cooled wall stabilises this mode. Although the cooling in our study is non-uniform, we similarly find that cooling the divergent section downstream of the throat reduces the amplification of this mode. When comparing the temperature sensitivity profiles of the two Mack modes, we find that they generally exhibit opposite trends with respect to wall temperature variations [30], although in some regions they exhibit similar behaviour, as also noted by Poulain et al. [21]. It is also interesting to note that Schneider [8] has observed a similar reduction in flow instability, achieved by increasing the wall temperature near the throat and cooling downstream. However, in their study, the main purpose of heating the throat was to mitigate the effects of surface roughness on transition. Nonetheless, the present work demonstrates that heating the wall at the throat also has a beneficial effect on the growth of linear instabilities.

5.1. Gradient validation

To validate the linear sensitivity results described above, we now prescribe a new wall temperature profile defined as $T_{wall} = T_{iso} - \epsilon (\nabla_T G^2) = T_{iso} - E \times (\nabla_T G^2/\mu^2)$ where ϵ (or equivalently $E = \epsilon \mu^2$) quantifies the intensity of the applied control. A new base-flow is then computed using this new temperature profile, and the resolvent analysis is repeated for the same (f, m) values. Fig. 6 (Left) shows the modified wall temperature profiles used for the new base-flows, while Fig. 6 (Right) shows the corresponding resolvent gains as a function of the control intensity. These gains are compared to the linear prediction provided by the sensitivity analysis: $G^2 = \mu^2 - \epsilon ||\nabla_T G^2||_{Q_T}^2$ (from Eq. (12) under the assumption of optimal control based on the direction of the sensitivity, i.e. $p = -\epsilon \nabla_T G^2$). The degree of agreement between the actual resolvent gain and the linear prediction indicates the validity of the linear sensitivity approximation. Significant deviations suggest the onset of nonlinear effects in the base-flow, leading to inaccuracies in the sensitivity estimate solely from the original uncontrolled base-flow.

For low control intensities *E* applied to the initial base-flow, we observe excellent agreement between the linear prediction and the new resolvent gain computed on the modified base-flows. This confirms the successful stabilisation of the mode and validates the wall-temperature sensitivity results, as the relative error between the prediction and the new resolvent value remains small. Additionally, the linear prediction remains accurate across a relatively wide range of control amplitudes for all three modes, even in cases involving strong control that results in significant gain reduction. This is a highly encouraging

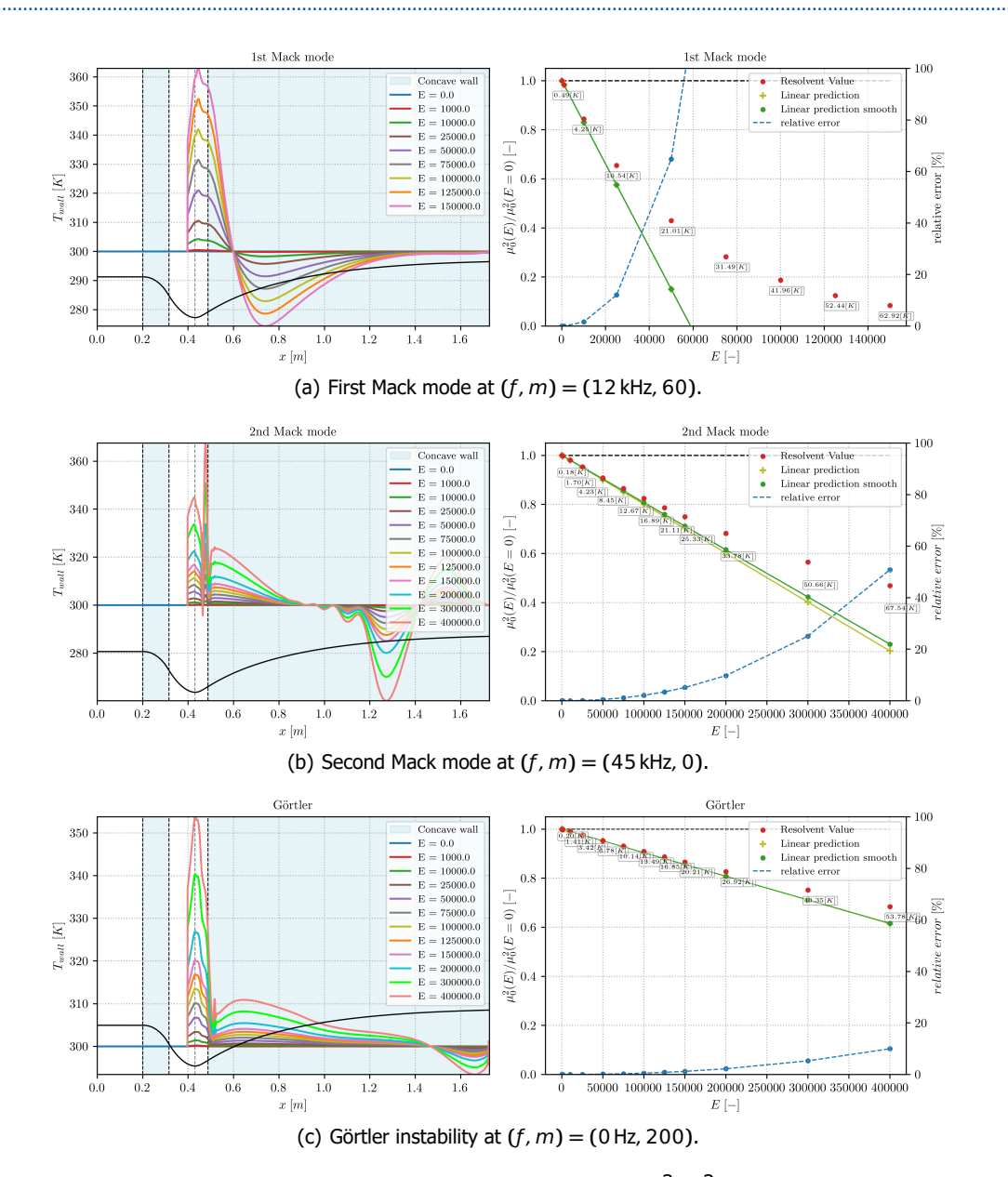


Fig 6. (Left): New nozzle wall temperature: $T_{wall} = T_{iso} - E(\nabla_T G^2/\mu^2)$, imposed to compute the new base-flows for the three dominant flow instabilities. (Right): Validation of the gradients obtained from the sensitivity analysis by comparing the linear prediction: $\mu^2(p=0) - \epsilon \|\nabla_T G^2\|_{Q_T}^2$ (with and without smoothing near the throat, see Fig. 5) to the new optimal resolvent gain computed on the modified base-flows (at the same (f,m)). The relative error is defined as the difference between the linear prediction and the computed resolvent gain. The temperature values indicated at each point correspond to the maximum temperature difference, ΔT_{max} , between the base-flow with and without control.

outcome for future nozzle optimisation efforts, as it suggests that convergence towards an optimal wall temperature distribution may require only a few optimisation iterations thanks to the ability to apply relatively large control values *E* without compromising prediction accuracy.

Interestingly, a given reduction of the optimal gain results in a relative deviation between the linear prediction and the real resolvent gain of similar magnitude across all three modes considered. For example, a gain reduction by a factor of 0.6 corresponds to a relative error of approximately 10% for each mode, as shown in Fig. 6. This observation suggests that nonlinear effects on the base-flow begin to manifest at a similar threshold of initial gain reduction, regardless of the specific mode analysed.

We also note that the smoothing applied to the sensitivity near the throat, introduced to address the irregular behaviour of the adjoint solution near the sonic line (see Appendix § 7.), results to only a negligible deviation in the computed gradient and therefore has minimal impact on the predicted reduction of the optimal resolvent gain. This smoothed sensitivity profile provides a more physically

realisable temperature distribution without compromising the accuracy or reliability of the sensitivitybased predictions.

5.2. Optimal profile designed to simultaneously control several unstable modes

In this section, our goal is to determine the optimal wall temperature profile to simultaneously reduce multiple modes. Using the sensitivity results obtained for each mode, we aim to define a gradient direction that effectively minimises the combined growth of these modes. To do this, we define a cost function that minimises the Euclidean norm of the combined ratios between the gains after and before wall-temperature control. A lower value of this cost function indicates a stronger overall reduction of the set of modes considered. However, it should be noted that there is no unique choice for such a cost function. In the present study, we propose two possible formulations:

$$\Delta T_{\text{optimal},i} = \arg \min_{\substack{\Delta T \leq \Delta T_{max} \\ r_{min} \leq (G_{\nu}^{2}/\mu_{\nu}^{2}), \ \forall k}} \mathcal{F}_{i}(\Delta T)$$
(15)

$$\Delta T_{\text{optimal},i} = \arg \min_{\substack{\Delta T \leq \Delta T_{max} \\ r_{min} \leq (G_k^2/\mu_k^2), \, \forall k}} \mathcal{F}_i(\Delta T)$$
with,
$$\mathcal{F}_1(\Delta T) = \sqrt{\sum_{k=1}^{N_{modes}} \left[\frac{G_k^2(\Delta T)}{\mu_k^2} \right]^2} \text{ or } \mathcal{F}_2(\Delta T) = \sqrt{\sum_{k=1}^{N_{modes}} N_k^2 \left[\frac{G_k^2(\Delta T)}{\mu_k^2} \right]^2}$$
and,
$$G_k^2(\Delta T) = \mu_k^2 + (\nabla_p G^2)_k^* Q_p \Delta T$$
(15)

The first definition \mathcal{F}_1 is the simplest form, it consists of minimising the Euclidean norm of the optimal gain ratios after and before control for the different modes. However, this approach does not take into account which modes are dominant in the flow. Thus, the optimisation tends to favour the most sensitive mode for a given maximum control intensity. Since it is more important to stabilise the instabilities that are responsible for the transition rather than simply the most sensitive modes, we propose to weight each term of the cost function by the N factor of the corresponding mode (see \mathcal{F}_2). This factor reflects the ability of each instability to trigger transition, thereby prioritising modes with greater physical impact. Regarding optimisation constraints, it was observed that errors from the linear sensitivity approach become significant when the instability is reduced by a factor of $r_{min} = 0.6$. Consequently, this value is chosen as the maximum allowable reduction for each mode. Moreover, since Mack's first mode is the most sensitive, this reduction factor corresponds to a maximum wall-temperature variation of approximately $\Delta T_{max} = 10 K$, which constitutes an additional constraint on the desired temperature profile. The two optimisation problems described above are solved using a trust-region method [31] implemented in scipy.minimize, which enables the incorporation of both constraints and bounds within the optimisation domain. The resulting temperature profiles after optimisation are shown in Fig. 7 using only the three dominant modes

Tab. 1 and Fig. 7 show that, in all cases, it is possible to find a solution that stabilises all the modes. As expected, the cost function \mathcal{F}_1 tends to locally favour the most sensitive mode of the flow. This highlights the advantage of \mathcal{F}_2 , which instead targets the dominant instability, even if it is less sensitive to control, as is the case for the Görtler instability in our configuration. In both cases, we observe that heating at the nozzle throat is required to stabilise the three dominant modes. This finding suggests that the heating commonly applied to the throat in quiet wind tunnels, primarily to mitigate the influence of roughness on transition by thickening the boundary layer, may also have the beneficial effect of mitigating the growth of these modes, thus helping to maintain laminar boundary layers over longer distances.

However, in our case, we observe that downstream of the nozzle throat, it is preferable not to modify the wall temperature if one wishes to avoid adversely affecting the dominant mode relative to the others. It is important to note that this conclusion strongly depends on the formulation of the optimisation problem, particularly the choice of the cost function \mathcal{F}_i . In this study, we focus only on wall-temperature control, but other control strategies could be considered, such as nozzle geometry optimisation. For example, future work could demonstrate that stabilising the Görtler instability may be more effectively achieved by acting solely on the geometry, given that this mode is directly linked to the concave curvature of the wall, whereas the first Mack mode might be better controlled via walltemperature adjustment, even if this slightly compromises the Görtler instability, which would remain primarily stabilised by geometric modifications of the nozzle.

Moreover, it would also be valuable to extend the analysis beyond the dominant modes alone, i.e. those corresponding to the peaks on the gain map, by also considering other frequencies and azimuthal

Fig 7. Optimal wall temperature profile designed to simultaneously control the maximum amplification of the Görtler instability and the first and second Mack modes using the cost function \mathcal{F}_1 and \mathcal{F}_2 . (—), (—) and (—) correspond to the maximum bounds of the optimisation problem for each mode.

	$(G^2/\mu^2)_{1\text{st mode}}$	$(G^2/\mu^2)_{2\text{nd mode}}$	$(G^2/\mu^2)_{\text{g\"ortler}}$
maximum bounds	0.595	0.886	0.928
using \mathcal{F}_1	0.596	0.887	0.946
using \mathcal{F}_1	0.689	0.920	0.928

Table 1. Optimal gain ratios after and before control for the different modes obtained after optimisation. The first row corresponds to the maximum bounds of the optimisation problem for each mode.

wavenumbers. This would ensure that the selected temperature profile effectively stabilises the entire gain map. Indeed, focussing exclusively on the dominant modes could inadvertently destabilise other previously less critical regions.

6. Conclusion

To conclude, the resolvent analysis enabled the identification of three dominant resolvent modes within the nozzle, encompassing the throat and divergent sections: the Görtler instability, along with the first and second Mack modes. Subsequently, a wall temperature sensitivity analysis was performed and validated for the three dominant modes within the nozzle. The results revealed that heating the wall near the throat effectively stabilises all three resolvent modes. However, further downstream, the different instability mechanisms begin to compete with each other. Among these modes, the first Mack mode exhibits the highest sensitivity to wall temperature variations. Using the sensitivity results, an optimal profile is also designed to simultaneously control several unstable modes. The resulting optimal profile for a new step of nozzle optimisation strongly depends on the definition of the cost function, and consequently on the relative priorities assigned to stabilising one mode versus another.

With additional validation as discussed in this paper, these sensitivity and optimal profile results could soon serve as optimal gradients to inform gradient-based optimisation strategies. However, appropriate constraints must be incorporated within the optimisation process to ensure the desired Mach number at the nozzle exit and maintain a uniform Mach profile at the model location. This constrained optimisation loop could then be employed to design a nozzle that effectively reduces instability growth, thereby delaying the onset of turbulent boundary layers, and therefore supporting the development of next-generation quiet wind tunnels and advanced ground testing facilities for hypersonic flows.

7. Appendix

The strong oscillations observed near the nozzle throat originate from perturbations generated at the root of the sonic line (close to the wall), which then propagate along characteristic lines, forming a "wave" pattern throughout the nozzle. This phenomenon can be observed in the sensitivity to volume forcing, $\nabla_{f_c}G^2$ (see Eq. (14)) illustrated for the second mode in Fig. 8 (similar waves also appear for the other modes). These perturbations near the throat are linked to the fact that the Jacobian matrix has a zero eigenvalue and becomes non-invertible, which no longer constrains certain components of the adjoint solution. This behaviour was previously identified in 1D nozzle analyses, where the adjoint was shown to be singular at the sonic line [32]. However, in 2D cases, the singularity vanishes except at locations where the streamlines are orthogonal to the sonic line. Such orthogonality is indeed observed

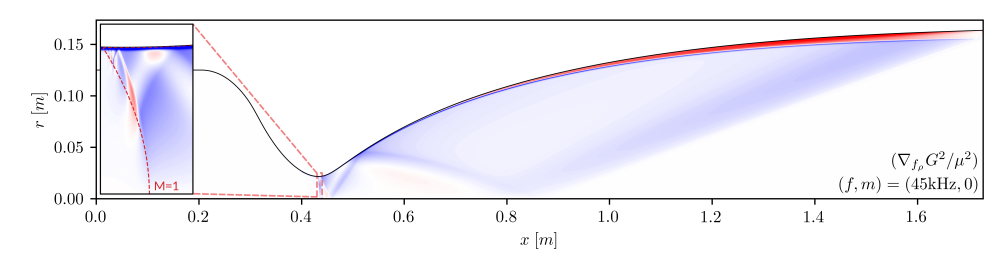


Fig 8. Sensitivity of the optimal resolvent gain for the second Mack mode to a volume forcing control $(\nabla_{f_c}G^2/\mu^2)$ (see Eq. (14)). Visualisation of the density component of the volume forcing control. For clarity, only the following contribution is shown: $-Q_{f_c}^{-1}P^*\mathcal{J}_0^{-1}*\frac{1}{\mu^2}(\partial_q(Q_E\check{q}_r))^*\check{q}_r$, which helps highlight the underlying physical mechanisms.

near the wall, as shown in Fig. 8. In practice, this behaviour may not represent a true singularity at the root of the sonic line but rather a steep gradient, a feature commonly observed in adjoint fields for transonic flow configurations [33, 34].

References

- 1. Schneider, S. P. Development of hypersonic quiet tunnels. Journal of Spacecraft and Rockets (2008).
- Morkovin, M. V. On the many faces of transition in Viscous Drag Reduction: Proceedings of the Symposium on Viscous Drag Reduction held at the LTV Research Center, Dallas, Texas (1969).
- 3. Laufer, J. Aerodynamic noise in supersonic wind tunnels. Journal of the Aerospace Sciences (1961).
- 4. Chazot, O. et al. Need for Low-Noise High-Speed Facilities in Europe in FAR (2019).
- 5. Beckwith, I. E., Chen, F.-J. & Creel JR, T. Design requirements for the NASA Langley supersonic low-disturbance wind tunnel in 14th aerodynamic testing conference (1986).
- 6. Saric, W. S. Görtler vortices. Annual Review of Fluid Mechanics (1994).
- 7. Xu, D., Ricco, P. & Duan, L. Görtler instability and transition in compressible flows. AIAA Journal 62, 489-517 (2024).
- Schneider, S. P. Design of a Mach-6 quiet-flow wind-tunnel nozzle using the e**N method for transition estimation in 36th AIAA Aerospace Sciences Meeting and Exhibit (1998).
- 9. Chen, F.-J., Malik, M. R. & Beckwith, I. E. Instabilities and transition in the wall boundary layers of low-disturbance supersonic nozzles in 18th Fluid Dynamics and Plasmadynamics and Lasers Conference (1985).
- 10. Schneider, S. P., Rufer, S., Randall, L. & Skoch, C. Shakedown of the Purdue Mach-6 quiet-flow Ludwieg tube in 39th Aerospace Sciences Meeting and Exhibit (2001).
- 11. Mack, L. M. Boundary-layer linear stability theory. Agard rep (1984).
- 12. Schneider, S. P. Design and fabrication of a 9.5-inch Mach-6 quiet-flow Ludwieg tube in 20th AIAA Advanced Measurement and Ground Testing Technology Conference (1998).
- 13. Benay, R. & Chanetz, B. Design of a boundary layer suction device for a supersonic quiet wind tunnel by numerical simulation. Aerospace science and technology (2004).
- 14. Marquet, O. e. a. Direct and adjoint global modes of a recirculation bubble: lift-up and convective non-normalities. JFM (2009).
- 15. Barbagallo, A. e. a. Closed-loop control of unsteadiness over a rounded backward-facing step. Journal of Fluid Mechanics (2012).
- 16. Schmid, P. J. Nonmodal stability theory. Annu. Rev. Fluid Mech. (2007).
- 17. Sipp, D. e. a. Dynamics and control of global instabilities in open-flows: a linearized approach. Appl. Mech. Rev. (2010).
- 18. Lakebrink, M. e. a. Optimization of a Mach-6 quiet wind-tunnel nozzle. Journal of Spacecraft and Rockets (2018).
- 19. Sipp, D. & Marquet, O. Characterization of noise amplifiers with global singular modes: the case of the leading-edge flat-plate boundary layer. Theoretical and Computational Fluid Dynamics (2013).
- 20. Marquet, O., Sipp, D. & Jacquin, L. Sensitivity analysis and passive control of cylinder flow. Journal of Fluid Mechanics (2008).
- 21. Poulain, A. et al. Adjoint-based linear sensitivity of a supersonic boundary layer to steady wall blowing–suction / heating–cooling. Journal of Fluid Mechanics 978, A16 (2024).
- 22. Mettot, C. Linear stability, sensitivity, and passive control of turbulent flows using finite differences PhD thesis (2013).
- 23. Lemarquand, H. et al. Transition mechanisms in hypersonic wind-tunnel nozzles: a methodological approach using global linear stability analysis. arXiv: 2504.16679 [physics.flu-dyn] (2025).
- 24. Kitzinger, E. Study of the boundary layer stability, receptivity, and control based on linearized chordwise-global analyses PhD thesis (Institut Polytechnique de Paris, 2023).
- 25. Poulain, A. et al. BROADCAST: A high-order compressible CFD toolbox for stability and sensitivity using Algorithmic Differentiation. Computer Physics Communications (2023).
- 26. Chu, B.-T. On the energy transfer to small disturbances in fluid flow (Part I). Acta Mechanica (1965).
- 27. Caillaud, C. et al. Separation and transition on a cone-cylinder-flare: computational investigations in AIAA SCITECH (2024).
- 28. Sipp, D. & Jacquin, L. Three-dimensional centrifugal-type instabilities of two-dimensional flows in rotating systems. PoF (2000).
- 29. Lescop, T. et al. Resolvent Analysis of Hypersonic Boundary Layer over Blunted Cones in HiSST (2025).
- 30. Mack, L. M. in Instabilities and turbulence in engineering flows 175-188 (Springer, 1993).
- 31. Byrd, R. e. a. A Trust-Region Method for Large-Scale Nonlinear Constrained Optimization. Mathematical Programming (2020).
- 32. Giles, M. & Pierce, N. Analytic adjoint solutions for the quasi-one-dimensional Euler equations. Journal of Fluid Mechanics (2001).
- 33. Giles, M., Pierce, N., Giles, M. & Pierce, N. Adjoint equations in CFD-Duality, boundary conditions and solution behaviour in 13th computational fluid dynamics conference (1997), 1850.
- 34. Lozano, C. Watch your adjoints! Lack of mesh convergence in inviscid adjoint solutions. AIAA Journal 57, 3991–4006 (2019).